THE JOURNAL OF PHYSICAL CHEMISTRY C

Article

Cite This: J. Phys. Chem. C 2019, 123, 28753−28762

pubs.acs.org/JPCC

Modulating Photoelectrochemical Water-Splitting Activity by Charge-Storage Capacity of Electrocatalysts

Yawen Dai,[†,‡] Ping Cheng,[†,§] Guancai Xie,[†,‡] Chengcheng Li,[∥] Muhammad Zain Akram,[†,‡] Beidou Guo,[†,‡] Rajender Boddula,[†] Xinghua Shi,*[,†,‡] Jinlong Gong,*[,∥] and Jian Ru Gong*[,†]

[†]Chinese Academy of Sciences (CAS) Center for Excellence in Nanoscience, CAS Key Laboratory of Nanosystem and Hierarchy Fabrication, National Center for Nanoscience and Technology, Beijing 100190, China

[‡]University of Chinese Academy of Sciences, Beijing 100049, China

[§]College of Science, University of Shanghai for Science and Technology, Shanghai 200093, China

[∥]Tianjin University, Tianjin 300072, China

Supporting Information

ABSTRACT: Electrocatalysts (ECs) are indispensable for high-efficiency photoelectrochemical (PEC) water splitting, but the underlying mechanism for performance modulation is still not clear. Taking the α-Fe_2O_3 semiconductor (SC) decorated with the cobalt oxide ECs as the model photoanode system, we demonstrate the opposite changes of PEC water oxidation activities by tuning the charge-storage capacity of ECs. Holes stored in the EC can increase the hole density on the photoanode surface, which can benefit the multihole surface water oxidation reaction, as well as aggravate the SC−EC interfacial charge recombination due to the Coulomb attraction. Both experimental and theoretical data prove that the EC with low hole-storage capacity brings limited interfacial charge recombination, enabling faster hole injection to improve the water oxidation activity. In contrast, the EC with high hole-storage capacity causes severe interfacial charge recombination, hindering the hole injection, thus decreasing the water oxidation activity. As a result, the PEC activity of photoanodes changes nonmonotonically with increasing surface hole density. This study can provide insightful guidance to interface design for solar energy-conversion systems.

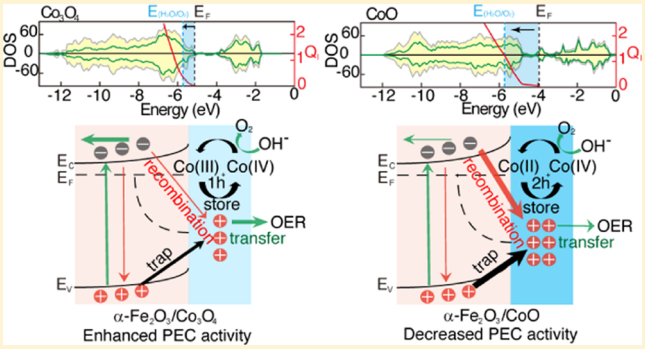

INTRODUCTION

Photoelectrochemical (PEC) water splitting over semiconductors (SCs) provides a potentially scalable approach to convert solar energy into clean and renewable H_2 fuel.[1−3] Electrocatalysts (ECs) are often deposited on SCs to promote the surface reaction during the PEC process.[4,5] However, integration of an EC with an SC cannot guarantee improved PEC performance since it changes the original SC−electrolyte interface into SC−EC and EC−electrolyte interfaces, complicating the relevant interfacial charge behavior, including interfacial charge transfer and recombination.[6] Therefore, understanding and modulating the interfacial charge behavior are pivotal for developing high-performance photoelectrodes.[7]

Significant progress has been made toward understanding the SC−EC−electrolyte interfaces in the PEC water-splitting system. Here, we focus on the photoanode, which is more challenging because the four-hole oxygen evolution reaction (OER) requires higher overpotentials.[8] Most currently reported efficient ECs for the OER are composed of oxides or (oxy)hydroxides of transition metals, which always have multiple valence states and pseudocapacitive characteristic, and thus ECs can store charges from SCs during the PEC process through the redox reactions of transition metal ions.[9−12] The hole-storage behavior of some ECs has been evidenced in various SC−EC composite photoanodes through complementary techniques, and it has been reported to have beneficial effects on the OER performance.[11,13−15] Boettcher's group demonstrates that the adaptive junction forms between SCs and ion-permeable ECs, in which the positive charges accumulated in ECs under the PEC condition increase the effective Schottky barrier height and the resultant photovoltage.[13] Li and co-workers suggest that an EC with hole-storage behavior can extract and store holes away from the SC, resulting in promoted charge separation and decreased photocorrosion in SCs.[12,16] Additionally, holes stored in ECs can increase the hole density on the photoanode surface, thus promoting the OER kinetics according to the rate law analysis on photoanodes.[17−19]

In the aforementioned works, only beneficial effects of ECs were reported, and the interfacial charge recombination

Received: September 2, 2019
Revised: October 24, 2019
Published: October 29, 2019

DOI: 10.1021/acs.jpcc.9b08343
J. Phys. Chem. C 2019, 123, 28753−28762

influenced by ECs, especially its negative effects, was omitted. It is suggested that the interface states between ECs and SCs can act as recombination centers, thus decreasing the PEC performance,[20] or an EC can slow the interfacial charge recombination as demonstrated by measuring the rate constants.[21] However, the underlying mechanism about how the interfacial charge behavior in the PEC system depends on ECs is still not clear. Besides, it was questioned whether the simple model for calculating the rate constant is valid for the complicated OER when an EC is involved.[22,23] Therefore, fundamental understanding of the EC-involved interfacial charge behavior is needed to better control the solar water-splitting performance.

Herein, we report a mechanism study of the influence of fundamental interfacial charge behavior on the PEC OER activity using the hematite (α-Fe_2O_3) photoanodes coated with Co-based ECs as a model system. Hematite is commonly used for the solar water-splitting mechanism studies because of its good stability, which can exclude the influence of self-corrosion during the PEC process.[24−27] The Co-based ECs employed here are Co_3O_4 and CoO nanoparticles with pseudocapacitive characteristic, and they have different hole-storage capacities due to their different Co valence states. Both ECs are active for the electrocatalytic OER, but they exert opposite effects on the PEC OER performance when coated on the hematite photoanodes. The performance changes are dominated by the competition between interfacial charge transfer and recombination that depends on the hole-storage capacities of ECs, as demonstrated through a combined experimental and theoretical study. This study suggests that the interfacial charge behavior and accordingly the solar water-splitting performance can be modulated by the hole-storage capacities of ECs, expanding the understanding and controlling of device interfaces for solar energy conversion.

EXPERIMENTAL AND THEORETICAL SECTION

Preparation of the α-Fe_2O_3 Films. The Ti-doped α-Fe_2O_3 films were synthesized by a hydrothermal method reported previously.[28] First, a solution of 0.05 M $FeCl_3{\cdot}6H_2O$ and 0.05 M Na_2SO_4 in 20 mL deionized water was prepared. Then, 0.3 mL of $TiCl_4$ solution (0.11 mL $TiCl_4$ + 10 mL ethanol) was added to the above solution. The mixed solution was transferred to a 50 mL Teflon-lined stainless-steel autoclave with a fluorine-doped tin oxide (FTO) substrate inside. Then, the autoclave was sealed and kept at 120 °C for 4 h to grow the FeOOH film. After growth, the film was rinsed with deionized water and dried with a N_2 flow. Finally, the sample was annealed at 600 °C for 1 h.

Synthesis and Dispersion of the ECs. For Co_3O_4 synthesis,[29] 2 mmol $Co(CH_3COO)_2{\cdot}4H_2O$ was dissolved in 20 mL of ethanol, into which 3.2 mL 25% $NH_3{\cdot}H_2O$ was added dropwise under vigorous stirring. The mixture was stirred in air for about 10 min and transferred into a 50 mL autoclave, sealed, and kept at 120 °C for 3 h. For CoO synthesis,[30] 1 mmol of cobalt(II) acetylacetonate (97% purity) was added to 28 mL of *tert*-butanol (≥99.7%). After stirring for about 10 min in air, the suspension was transferred into a 50 mL autoclave, sealed, and kept at 190 °C for 12 h. In both cases, the obtained precipitate was centrifuged at 8000 rpm for 5 min, followed by rinsing three times in ethanol. Finally, Co_3O_4 or CoO nanoparticles were dispersed in an acetic acid/ethanol solution (volume ratio = 7/3) by sonication.

Preparation of EC/α-Fe_2O_3 Composite Photoanodes. The Co_3O_4 or CoO nanoparticles were integrated to hematite films through a simple spin-coating process. Briefly, 30 μL of Co_3O_4 or CoO dispersion was dropped onto the hematite films, and spin coated at 1000 rpm for 10 s, followed by 3000 rpm for 30s. Then, the obtained samples were dried at 100 °C for 1 h. To eliminate the difference caused by the acetic acid/ethanol solution, the bare hematite was treated by the acetic acid/ethanol solution without EC through the same process described above to serve as a control.

Material Characterizations. X-ray diffraction (XRD) patterns were recorded on an X'Pert PRO MPD diffractometer with Cu Kα radiation (λ = 1.5405 Å). Raman spectra were collected with a Raman Microscope (Renishaw inVia plus) with a laser power of 0.5 mW and an excitation wavelength of 633 nm. A Hitachi-SU8220 field emission scanning electron microscope (SEM) at an accelerating voltage of 10 kV was used to characterize the micromorphology of the samples. An FEI Tecnai G2 F20 U-TWIN transmission electron microscope (TEM) operated at 200 kV was used to examine the micromorphologies and crystal structures of the samples. X-ray photoelectron spectroscopy (XPS) and valence band spectra measurements were performed on a Thermo Scientific ESCALAB 250 Xi system. The absorptance spectra were measured by using a UV-2600 spectrophotometer equipped with an integration sphere, and the absorptance of the sample was calculated by the formula $A = 1 - T - R$, where T is the transmittance and R is the reflectance. In the measurements, the sample was positioned at the frontside for collecting transmittance data and at the backside for collecting reflectance data. Photoluminescence (PL) spectra were collected on a photoluminescence spectrometer (NanoLOG-TCSPC) with an excitation wavelength of 440 nm.

Photoelectrochemical Characterization. Photoelectrochemical measurements were performed at room temperature in a three-electrode configuration on an electrochemical workstation (Zahner Zennium, Germany), with a prepared photoanode as the working electrode, a saturated Ag/AgCl electrode as the reference electrode, a Pt foil as the counter electrode, and 1 M NaOH aqueous solution (pH = 13.6) as the electrolyte. The light source was a 500 W xenon lamp (CEL-S500, Aulight, Beijing, China) equipped with an AM 1.5G filter, and the distance from the light source to the samples was adjusted to realize an irradiation of 100 mW cm^{-2} (1 sun). The samples were irradiated from the backside for all of the tests. The current density−applied potential (J−V) plots of the photoanodes were measured at a scanning rate of 17 mV s^{-1}. Photovoltages were measured by recording the open-circuit potentials under light and in the dark. Intensity-modulated photocurrent spectroscopy (IMPS) was conducted with a Zahner CIMPS system under continuous illumination from a white light-emitting diode (100 mW cm^{-2}). IMPS response was collected using a 7% light intensity modulation over a frequency range from 10 kHz to 0.1 Hz. The photoelectrochemical impedance spectroscopy (PEIS) data were gathered under 1 sun irradiation using a 5 mV amplitude perturbation between 100 kHz and 0.1 Hz without setting any stabilization time and the data were fitted using Zview software. The error bars in IMPS and PEIS are calculated by the formula of sample standard deviation(s), $s = \sqrt{(\sum_{i=1}^{n}(x_i - \bar{x})^2)/(n-1)}$, where x_i refers to the

DOI: 10.1021/acs.jpcc.9b08343
J. Phys. Chem. C 2019, 123, 28753−28762

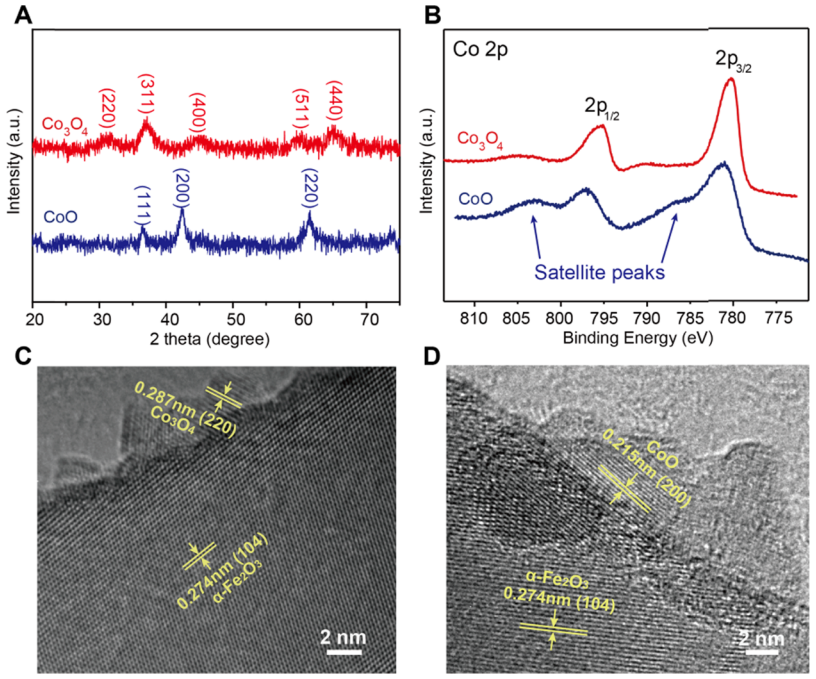

Figure 1. (a) XRD patterns and (b) XPS spectra of Co 2p for Co_3O_4 and CoO. High-resolution transmission electron microscopy images of (c) α-Fe_2O_3/Co_3O_4 and (d) α-Fe_2O_3/CoO.

measured or fitted value of samples, $\bar{x}$ stands for the mean value of samples, and n represents the number of samples.

Computational Details. First-principle density functional theory (DFT) calculations were performed using the Vienna ab initio simulation package (VASP).[31−33] The projector augmented wave (PAW) method implemented by Kresse et al. was used to calculate the electronic and atomic structures of all of the systems studied here.[34] Exchange−correlation effects were treated in generalized gradient approximation (GGA) with the Perdew−Burke−Ernzerhof (PBE) potential.[35] To eliminate 3d-state self-interaction error of Co atoms, the DFT + U method[36,37] with an effective Hubbord parameter ($U_{eff} = U - J$) of 3.70 eV was applied to Co atoms in our calculation. The kinetic energy cutoff was chosen to be 500 eV. Brillouin zone integration was sampled with 6 × 6 × 6 Monkhorst−Pack mesh K-points for the bulk Co_3O_4 and CoO relaxation. For the (110), (100), and (111) surface systems of Co_3O_4 and CoO, 3 × 3 × 1 K-points were used for the relaxations and 5 × 5 × 1 K-points were used for the electronic property calculations. A vacuum region of 15 Å was used for the surface systems to eliminate the interaction of periodic images of the systems. Gaussian smearing method[38] with a width of 0.05 eV was employed to determine electron occupancies. During optimization, the minimizing force acting on each atom was less than 0.01 eV $Å^{-1}$ and the convergence of energy was set to 10^{-5} eV.

RESULTS AND DISCUSSION

The α-Fe_2O_3/EC photoanodes were prepared by spin coating Co_3O_4 or CoO ECs onto the α-Fe_2O_3 photoanode, which has a Ti-doped worm-like nanostructure (Figures S1 and S2) made by a facile method.[28] For single EC, the X-ray diffraction (XRD) peaks at 31.2, 36.9, 44.8, 59.9, and 65.0° are assigned to the (220), (311), (400), (511), and (440) planes of spinel Co_3O_4, and the peaks at 36.5, 42.4, and 61.5° are designated to the (111), (200), and (220) planes of rock salt CoO, respectively (Figure 1a).[39] The EC identifications are also confirmed by the Raman spectra (Figure S3a).[39] The valence states of Co in the ECs are analyzed by X-ray photoelectron spectroscopy (XPS) (Figure 1b). Co_3O_4 shows the binding energies of Co $2p_{3/2}$ and Co $2p_{1/2}$ located at 780 and 795 eV, and small satellite peaks are observed (Figure 1b), indicating the dominant valence state of Co(III). In comparison, CoO shows ∼1 eV higher binding energy values of Co $2p_{3/2}$ and Co $2p_{1/2}$ and much stronger satellite peaks at 786 and 803 eV (Figure 1b), which correspond to the feature peaks of Co(II).[40] The dominant valence states of Co(III) in Co_3O_4 and Co(II) are also confirmed by the cyclic voltammogram (CV) technique (Figure S3b).[41,42] Additionally, the non-rectangular shapes of the CV curves (Figure S3b) display that the two ECs have pseudocapacitive charge-storage characteristics originating from reversible redox reactions.[43] XRD patterns of the α-Fe_2O_3, α-Fe_2O_3/Co_3O_4, and α-Fe_2O_3/CoO samples (Figure S3c) show the characteristic diffraction peaks of α-Fe_2O_3, and no signal of Co_3O_4 or CoO is observed due to the tiny loading amount. However, both XPS Fe 2p spectra and CV diagrams of α-Fe_2O_3/Co_3O_4 and α-Fe_2O_3/CoO samples suggest the decent coverage of the electrocatalysts on the surface of the nano hematite (Figure S3d,e). Scanning electron microscopy (SEM) images (Figure S2a−c) display that both modified α-Fe_2O_3 photoanodes preserve the morphology similar to that of the bare α-Fe_2O_3. Transmission electron microscopy (TEM) images (Figures 1c,d and S2d−f) show the surface of α-Fe_2O_3 decorated by irregularly shaped nanoparticles of Co_3O_4 and CoO ECs, which have similar morphology and size range of 4−10 nm.

α-Fe_2O_3/Co_3O_4 and α-Fe_2O_3/CoO containing the same mass of Co element were used as the model samples for the in-depth study after tuning the amount of EC loading (Figure S4). The α-Fe_2O_3/Co_3O_4 photoanode shows a cathodically shifted photocurrent onset potential from 0.99 to 0.92 V_{RHE} (volts versus reversible hydrogen electrode), and an increased

DOI: 10.1021/acs.jpcc.9b08343
J. Phys. Chem. C 2019, 123, 28753−28762

photocurrent density from 0.82 to 1.31 mA cm^{-2} at 1.23 V_{RHE} compared to the bare α-Fe_2O_3 (Figure 2). In contrast, α-Fe_2O_3/CoO shows an anodically shifted onset potential of 1.07 V_{RHE} and a decreased photocurrent density of 0.41 mA cm^{-2} at 1.23 V_{RHE} (Figure 2). Here, the photocurrent onset potential is calculated by extrapolating the linear portion of the $J-V$ curves to zero current.[44] The small photocurrent density (below 0.2 mA cm^{-2}) of α-Fe_2O_3/CoO sustained from 0.75 to 1.07 V_{RHE} is a charging current due to the oxidation of Co(II) to Co(III) rather than water oxidation current,[45] which can be indicated by the zero steady-state photocurrent before 1.1 V_{RHE} (blue hollow symbols in Figure 2) read from the chronoamperometry (CA) measurements (Figure S5a–c). The above results demonstrate that Co_3O_4 and CoO have opposite effects in the PEC OER activity after modifying the α-Fe_2O_3 photoanodes (Figure 2). To ensure the reproducible behavior of the three electrodes, $J-V$ plots of more than three batches of independently prepared samples were tested, and the samples from all batches disclosed consistent results (Figures S6a and S7a).

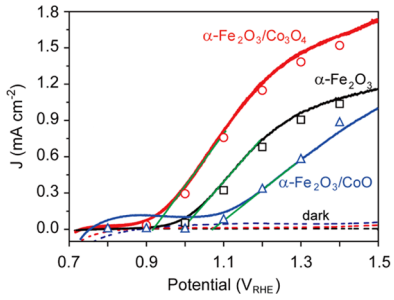

Figure 2. Photocurrent densities of α-Fe_2O_3/Co_3O_4, α-Fe_2O_3/CoO, and α-Fe_2O_3 under 1 sun irradiation. The solid lines indicate the $J-V$ curves recorded from linear sweep voltammetry with a scan rate of 17 mV s^{-1}. The hollow symbols stand for the steady-state photocurrent densities recorded from the CA measurements, which exclude the charging current. The dashed lines represent the corresponding dark current densities of all of the photoanodes. The green lines indicate the extrapolation from the linear portion of the $J-V$ curves to zero current for the onset potential determination.

To investigate the underlying reason for the opposite changes in the PEC OER activity caused by different EC modification, a thorough thermodynamic (light absorption and photovoltage) and kinetic (electrocatalytic activity, bulk, and interfacial charge transfer/recombination) analysis was carried out.

UV–visible absorptance spectra (Figure S8a) indicate that the EC-coated α-Fe_2O_3 photoanodes show negligible difference in light absorption compared to the bare one. Both ECs can form p–n junctions with α-Fe_2O_3 (Figure S8a–f), and thus the photovoltages of α-Fe_2O_3/Co_3O_4 and α-Fe_2O_3/CoO are higher compared to the bare one (Figure S9a). The OER electrocatalytic activity of Co_3O_4 and CoO evaluated from $J-V$ curves and EIS in the dark (Figure S9b,c) indicates that both ECs are dramatically more active than the bare α-Fe_2O_3. The bulk charge recombination process was detected by photoluminescence (PL) emission spectra (Figure S9d). The PL peak at 584 nm (2.1 eV) consistent with the band gap value (Figure S8b) of α-Fe_2O_3 is assigned to the interband charge recombination. The slightly weakened PL intensity after coating Co_3O_4 and CoO implies that both ECs suppress the bulk charge recombination in α-Fe_2O_3 to a similar extent.

In a word, both ECs do not change the light absorption of α-Fe_2O_3. The effects of both ECs on photovoltage, electrocatalytic activity, and bulk charge recombination are beneficial for improving the PEC OER activity, which is inconsistent with the opposite activity changes induced by Co_3O_4 and CoO. Additionally, due to the similar size and morphology of the two ECs, the tiny loading amount, as well as the spin-coated α-Fe_2O_3–EC interfaces without facet-selective adsorption, the influence of interface states at the α-Fe_2O_3–Co_3O_4 and α-

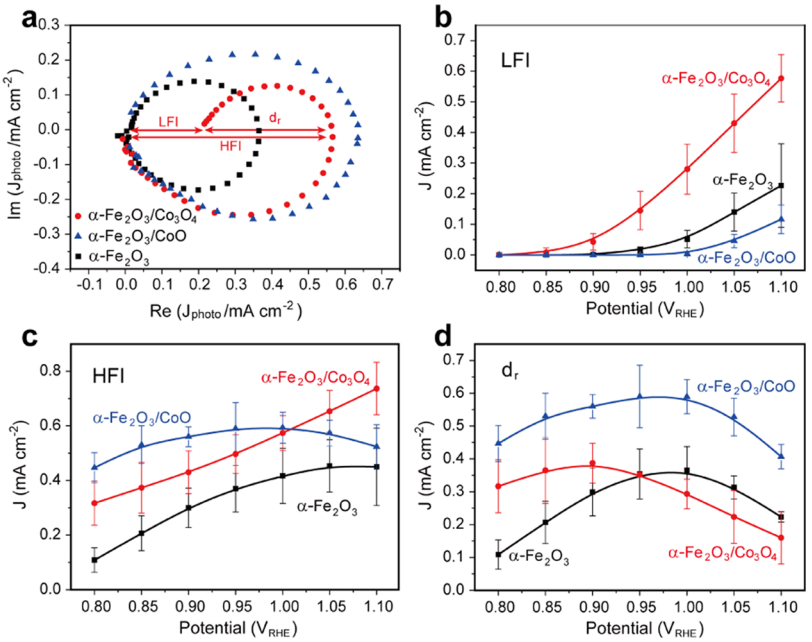

Figure 3. (a) IMPS complex plots at 0.95 V_{RHE} of the α-Fe_2O_3/Co_3O_4, α-Fe_2O_3/CoO, and α-Fe_2O_3 photoanodes. (b) LFIs, (c) HFIs, and (d) d_r of the IMPS response from 0.8 to 1.1 V_{RHE} of the α-Fe_2O_3/Co_3O_4, α-Fe_2O_3/CoO, and α-Fe_2O_3 photoanodes. The error bars are representative of three independent experiments. Solid lines are guides to the eye.

DOI: 10.1021/acs.jpcc.9b08343
J. Phys. Chem. C 2019, 123, 28753–28762

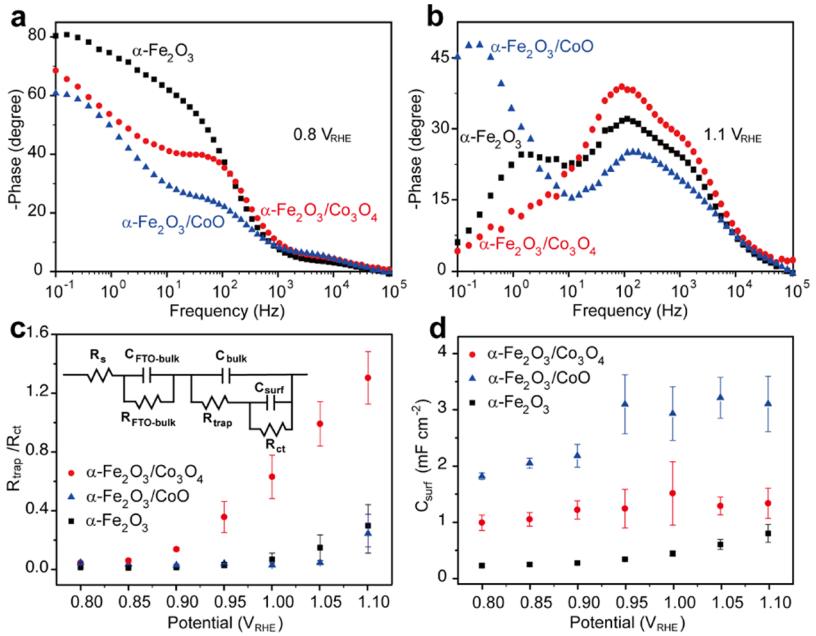

Figure 4. (a) PEIS−Bode plots at (a) 0.8 and (b) 1.1 V_{RHE} under 1 sun irradiation; PEIS fitting results of (c) R_{trap}/R_{ct} and (d) C_{surf} for α-Fe_2O_3/Co_3O_4, α-Fe_2O_3/CoO, and α-Fe_2O_3. The error bars are representative of three independent experiments.

Fe_2O_3−CoO interfaces can be regarded as similar. Therefore, the above factors can be excluded as the determinant reason for the PEC OER activity changes.

Next, we studied the interfacial charge behavior by IMPS and PEIS. The photoanodes keep their original J−V behaviors (Figures S6a and S7a) and Co valence states (Figure S7b) after the tests. This good sample stability ensures the validity of our analysis.

IMPS measurements were performed to directly detect the surface hole current and recombination current of the photoanodes under working conditions. The small-amplitude modulation of the light intensity alters only the surface charge concentration but not the band bending degree of the semiconductor, providing valid probe of the charge carrier behavior.[21] The IMPS response from 0.8 to 1.1 V_{RHE} (Figure S6b−d) was collected aiming at explaining the different irradiated J−V behavior of the bare and modified electrodes around their onset potentials. Figure 3a shows the representative IMPS spectra at 0.95 V_{RHE}. Each IMPS spectrum is composed of two semicircles distributed above and below the real axis with two intercepts. The low-frequency intercept (LFI) accounts for the steady-state photocurrent, which is determined by charge transfer across the photoanode−electrolyte interface.[23] The high-frequency intercept (HFI) generally corresponds to the hole flux toward the photoanode surface since the surface recombination is supposed to be frozen out at sufficiently high frequency.[20,23] The diameter (d_r) of the upper semicircle (also called recombination semicircle) indicates the surface recombination current of electrons from the SC conduction band and holes on the surface.[23]

The LFIs at different potentials (Figure 3b) agree well with the corresponding photocurrent densities read from the J−V plots measured under the same light source as in the IMPS test (Figure S6a), confirming the reliable assignment of the LFIs. As implied by the HFIs (Figure 3c), for the bare α-Fe_2O_3 and α-Fe_2O_3/Co_3O_4, the hole currents increase with potential, which is due to the decreasing charge recombination in the space-charge region with the increasing potentials.[46] For α-Fe_2O_3/CoO, the HFI increases with potential before 1.0 V_{RHE}, and then slightly decreases with potential from 1.0 to 1.1 V_{RHE}. This might be ascribed to the fast interfacial charge recombination at the α-Fe_2O_3−CoO interface, which is not completely frozen out, resulting in the measured HFI values smaller than that of the practical hole flux.[20] The EC-coated photoanodes show higher hole flux compared to the bare one, demonstrating more pronounced band bending and thus less charge recombination in the space-charge region of α-Fe_2O_3 since the rapid hole transfer from α-Fe_2O_3 to ECs,[46] which is also consistent with the increased photovoltage after coating ECs (Figure S9a).[13]

The d_r values of all three photoanodes are exhibited in Figure 3d as a measure of surface charge recombination. At low potentials, the recombination currents of all samples increase with potential, displaying the same trend as the hole flux. This is because all of the holes reaching the photoanode surface recombine with electrons at low potentials. Further increasing the applied potentials gradually reduces the surface charge recombination. Compared to the bare α-Fe_2O_3, α-Fe_2O_3/Co_3O_4 shows higher recombination currents before 0.95 V_{RHE} and slightly lower recombination currents thereafter. In contrast, α-Fe_2O_3/CoO sustains the highest recombination current in the whole potential range. In a word, coating CoO greatly increases the surface charge recombination, whereas coating Co_3O_4 shows relatively smaller influence on the surface charge recombination.

Then, PEIS measurements were carried out to shed light on the limiting process of the PEC OER activity.[47] The frequency value of each peak in PEIS−Bode plots reflects the time scale of the relevant process, and the phase value helps to identify the limiting process.[56] Three peaks in the Bode plots (Figure 4a,b) are observed for all of the examined electrodes. The peaks centered at the high (2000−5000 Hz), middle (50−100 Hz), and low frequencies (0.1−1.5 Hz) are assigned to charge transport across the FTO-α-Fe_2O_3 interface, within the bulk α-Fe_2O_3, and across the electrode−electrolyte interface,

DOI: 10.1021/acs.jpcc.9b08343
J. Phys. Chem. C 2019, 123, 28753−28762

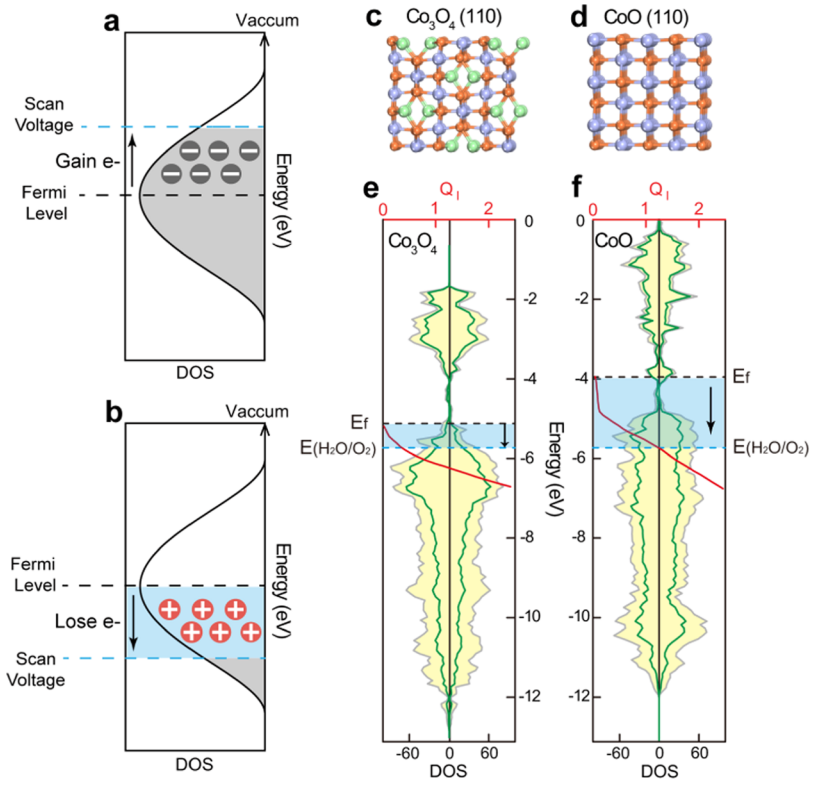

Figure 5. Schematic illustration of the (a) negative and (b) positive charge-storage processes. Ball and stick models with a top view of (c) Co_3O_4 (110) and (d) CoO (110); purple, green, and orange balls indicate Co^{2+}, Co^{3+}, and O^{2-} ions, respectively. DFT calculation results of (e) Co_3O_4 (110) and (f) CoO (110) facets. The total DOS (gray lines) and the PDOS of Co d-orbitals (green lines) are referenced to the vacuum level. The red lines indicate the integral PDOS of Co d-orbitals from the Fermi levels (E_f). The light blue regions from the E_f to the OER potential indicate the PDOS integration ranges to determine the hole-storage capacity.

respectively.[47,48] At 0.8 V_{RHE} (Figure 4a), all of the examined electrodes show the highest peak phase value at low frequency (<1 Hz), suggesting that charge transfer at the electrode−electrolyte interface is the limiting process. At 1.1 V_{RHE} (Figure 4b), for both α-Fe_2O_3 and α-Fe_2O_3/Co_3O_4, the peaks at the low frequency (~1.5 Hz) reduce and those at the middle frequency (~100 Hz) predominate, suggesting that the OER performance is limited by the bulk property of the electrodes. In contrast, α-Fe_2O_3/CoO still shows the highest phase value at the low frequency (~0.2 Hz), implying that charge transfer at the electrode−electrolyte interface is the limiting process in the whole tested potential range. Moreover, the corresponding peak frequency value of α-Fe_2O_3/CoO (~0.2 Hz) is even smaller than that of the bare α-Fe_2O_3 (~1.5 Hz), suggesting a slower charge-transfer rate from the electrode to the electrolyte after CoO coating. Given that CoO is an active EC for the OER (Figure S9b,c), the blocked charges at the α-Fe_2O_3−CoO interface could be the reason for the slower charge transfer.

The PEIS data are fitted to extract charge-transfer resistances and capacitances at different interfaces. The equivalent circuit (Figure 4c, inset) used for the PEIS fitting is established on the basis of the widely reported reaction mechanism for hematite-based photoanodes.[11,47,49] Under low potentials around the photocurrent onset, holes are trapped and stored in the surface states for a bare photoanode or in the EC for an EC-coated photoanode before a threshold of the surface hole density for the OER is reached.[11,49] The processes can be modeled by a hole-trapping resistance toward the photoanode surface, R_{trap}, a surface capacitance coming from the hematite surface states or ECs, C_{surf}, and a charge-transfer resistance from the electrode to the electrolyte, R_{ct}.

The competition between the interfacial charge transfer and recombination is interrogated by comparing R_{trap} and R_{ct}. The ratio of R_{trap}/R_{ct} is proportional to the ratio of charge transfer and recombination rate constants (k_{ct}/k_{rec}), and thus this ratio value provides insights into the kinetics of charge transfer competing with charge recombination at the electrode−electrolyte interface.[50] Compared to the bare α-Fe_2O_3, α-Fe_2O_3/Co_3O_4 shows increased R_{trap}/R_{ct} values (Figure 4c), in accordance with the improved photocurrent and lower onset potential, implying that charge transfer outcompetes charge recombination in α-Fe_2O_3/Co_3O_4 to a greater extent than that in the bare α-Fe_2O_3.[20] In contrast, the low R_{trap}/R_{ct} values of α-Fe_2O_3/CoO indicate that the fast charge recombination at the α-Fe_2O_3−CoO interface inhibits the OER, causing a late-onset potential and a low photocurrent density.[20] The shapes of the R_{trap}/R_{ct} values as a function of applied potentials for both the bare and modified electrodes resemble the general trend of their corresponding J−V curves (Figure 2), and this agreement indicates that the PEC J−V behavior is determined by the competition between the interfacial charge transfer and recombination process.

To reveal how the interfacial charge behavior depends on the EC property, the hole-storage behavior of the ECs was scrutinized. The surface hole concentrations of the three electrodes are characterized by C_{surf} values from PEIS fitting (Figure 4d), and a variation trend of C_{surf} (α-Fe_2O_3/CoO) > C_{surf} (α-Fe_2O_3/Co_3O_4) > C_{surf} (α-Fe_2O_3) is observed, indicating the hole-storage behavior of the two ECs. The

DOI: 10.1021/acs.jpcc.9b08343
J. Phys. Chem. C 2019, 123, 28753−28762

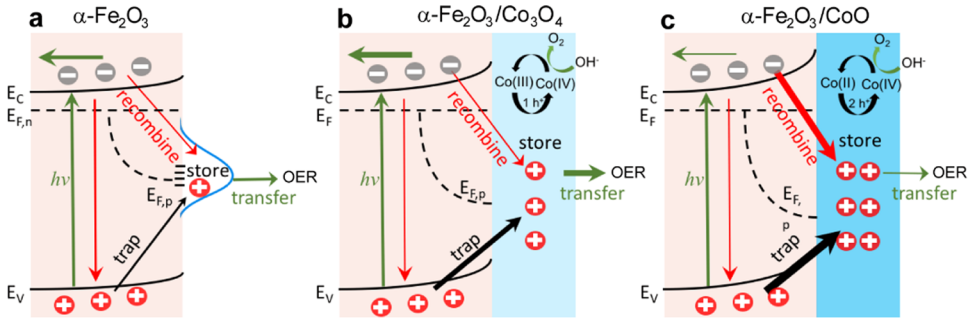

Figure 6. Illustration of the interfacial charge behavior under irradiation at a potential in the range of 0.8−1.1 V_{RHE} for the (a) α-Fe_2O_3, (b) α-Fe_2O_3/Co_3O_4, and (c) α-Fe_2O_3/CoO photoanodes. Green arrows refer to the beneficial contributions including charge generation from photoexcitation, electron transport to the substrate, and hole transfer to the electrolyte. Red arrows refer to the deleterious contributions including photogenerated charge recombination in the bulk and at interfaces. The black arrows refer to the hole trapping toward the photoanode surface. The arrow line thickness indicates the relative rates of charge transfer and recombination, and the thicker arrow lines represent the faster rates than the thinner ones.

large C_{surf} (α-Fe_2O_3/CoO) value is consistent with the significant charging current of the α-Fe_2O_3/CoO photoanode as displayed in Figure 2. The surface hole densities (Q) calculated from the negative current transients under chopped light condition (Figure S5) also exhibit a variation trend of $Q(\alpha\text{-}Fe_2O_3/CoO) > Q(\alpha\text{-}Fe_2O_3/Co_3O_4) > Q(\alpha\text{-}Fe_2O_3)$, which coincides with the results from the C_{surf} measurement. These results demonstrate that both Co_3O_4 and CoO can store holes from α-Fe_2O_3, and CoO exhibits a larger hole-storage capacity than Co_3O_4.

The different hole-storage capacity of the two ECs can be ascribed to their different band bendings or their different valence states of Co. The built-in electric field in the EC due to band bending can store holes and may contribute to the observed difference in hole-storage capacity. However, as both CoO and Co_3O_4 nanoparticles have very small sizes of around 5 nm, so the band bending is negligible in CoO and Co_3O_4 nanoparticles with such small sizes,[51] which is further supported by band diagram simulations in α-Fe_2O_3/Co_3O_4 and α-Fe_2O_3/CoO heterojunctions (Figure S10 and Table S1). It can thus be confirmed that the capacitance effect of ECs is not related to their band bending. Therefore, the hole-storage behavior of Co-based ECs can be interpreted as Co(II) or Co(III) being oxidized by the photogenerated holes from α-Fe_2O_3, and holes are stored as Co(IV) in the ECs, as reported by the previous hematite−CoPi system.[11] Meanwhile, it has been confirmed that Co-based ECs catalyze the OER through a Co(IV) intermediate.[52,53] One hole is accepted for each Co(III) site to reach Co(IV), while two holes for each Co(II) site, thus resulting in the valence state-dependent hole-storage capacity.

A DFT calculation was performed to further explain the different charge-storage capacities between Co_3O_4 and CoO. The intrinsic charge-storage capacity of a pseudocapacitive material can be indicated by the density of states (DOS) between the original Fermi level and the external scan voltage.[54,55] Gaining electrons in the unoccupied orbitals above the Fermi level corresponds to reducing the transition metal atoms and storing negative charges (Figure 5a), whereas losing electrons in the occupied orbitals below the Fermi level corresponds to oxidizing the transition metal atoms and storing positive charges (Figure 5b). In our system, the two ECs are coated on the hematite photoanode, storing positive charges, and catalyzing the OER, and thus the number of electrons lost per Co atom (Q_l) was calculated by integrating the projected DOS (PDOS) of Co d-orbitals from the original Fermi level to the OER potential. The calculated DOS of the two materials should be referenced to the vacuum level to enable direct comparison with the externally applied voltages, and it is possible to calculate the vacuum level only for lattice planes but not for bulk models.[54,56] Therefore, we did the calculation on representative lattice planes rather than the bulk models. Additionally, the spin-coated ECs are irregularly shaped nanoparticles without certain facet exposure. Hence, (110) (Figure 5c,d), (100) (Figure S11a,b), and (111) (Figure S11c,d) facets of both Co_3O_4 and CoO are selected as the study model due to their good stability and catalytic activity.[57,58] The Fermi level of Co_3O_4 (110) is calculated to be −5.12 eV (Figure 5e). In comparison, CoO (110) shows a higher Fermi level of −3.95 eV (Figure 5f), corresponding to more occupied PDOS of Co atoms, which is consistent with the lower Co valence state in CoO than that in Co_3O_4. As a result, the Q_l value of CoO (1.2) is higher than that of Co_3O_4 (0.4). Furthermore, the averaged Q_l values over the three selected facets are 1.2 for CoO and 0.7 for Co_3O_4 (Table S2), confirming the larger hole-storage capacity of CoO than that of Co_3O_4, agreeing well with the experimental observation.

On the basis of the above analysis, the opposite effect of Co_3O_4 and CoO on the PEC OER activity of the α-Fe_2O_3-based photoanodes can be understood now. For the unmodified photoanode (Figure 6a), the photogenerated holes are trapped and stored in the surface states of α-Fe_2O_3. After coating an EC, the surface states of α-Fe_2O_3 are passivated, and a more favorable path for hole storage is provided,[26] resulting in a higher surface hole density compared to that of the bare one (Figure 6b,c). The two ECs exhibit different hole-storage capacity, which can be ascribed to their different Co valence states. The accumulated surface holes on photoanodes can promote the PEC OER kinetics,[19,59] but it can also lead to interfacial charge recombination due to the Coulomb attraction, thus leading to a nonmonotonic variation trend of the OER activity with increasing surface hole density (Figure S12). When coating Co_3O_4 on α-Fe_2O_3 (Figure 6b), the C_{surf} is enhanced to an optimal state, where it induces relatively limited interfacial charge recombination, and thus the increased surface reaching holes can be efficiently utilized for the OER, resulting in the promoted OER activity. However, when the C_{surf} is further increased as in the case of α-Fe_2O_3/CoO (Figure 6c), the highly concentrated holes in the EC cause a fast SC−EC interfacial charge recombination, which

DOI: 10.1021/acs.jpcc.9b08343
J. Phys. Chem. C 2019, 123, 28753−28762

inhibits hole transfer to the electrolyte, thus decreasing the OER activity. A similar nonmonotonic photoactivity variation trend dominated by the interfacial charge behavior was also demonstrated in another solar water-splitting system,[60] indicating that the above mechanism analysis is reasonable.

CONCLUSIONS

In summary, taking the α-Fe_2O_3 SC coated by two cobalt oxide ECs as a model system, we demonstrate the EC's hole-storage capacity-dependent PEC OER activity as proved by both experimental and theoretical data. ECs can store holes from the SC, thus increasing the surface hole density on the photoanode. The OER activity changes nonmonotonically with increasing surface hole density. For α-Fe_2O_3/Co_3O_4, the low hole-storage capacity of Co_3O_4 leads to limited interfacial charge recombination and thus benefits the surface hole utilization for the OER. In contrast, for α-Fe_2O_3/CoO, CoO shows a large hole-storage capacity that exceeds the optimal state and induces severe SC−EC interfacial charge recombination, thus hindering the charge transfer for the OER. As a result, the OER activity of the α-Fe_2O_3 photoanode is improved by Co_3O_4 but decreased by CoO. Therefore, the EC's hole-storage capacity is critical in governing the competition between interfacial charge transfer and recombination, thus determining the OER activity of the EC-modified photoanodes. These results provide a new strategy of tuning the interfacial charge behavior, allowing further development of more efficient devices for solar energy conversion.

ASSOCIATED CONTENT

Supporting Information

The Supporting Information is available free of charge on the ACS Publications website at DOI: 10.1021/acs.jpcc.9b08343.

Additional data for XPS, SEM, TEM, and XRD of the photoanodes, Raman and CV curves of Co_3O_4- and CoO-coated FTO, $J-V$ curves of α-Fe_2O_3 coated by different amounts of Co_3O_4 and CoO, chopped light chronoamperometry measurements, full IMPS complex plots, $J-V$ curves before and after the IMPS test, $J-V$ curves before and after the PEIS test, Bode plots and the corresponding fitted lines, UV−visible absorptance spectra, valence band region of the XPS spectrum, dark $J-V$ plots, OCP, and PL (PDF)

AUTHOR INFORMATION

Corresponding Authors

*E-mail: shixh@nanoctr.cn (X.S.).
*E-mail: jlgong@tju.edu.cn (J.G.).
*E-mail: gongjr@nanoctr.cn (J.R.G.).

ORCID

Ping Cheng: 0000-0002-3291-5200
Rajender Boddula: 0000-0001-8533-3338
Jinlong Gong: 0000-0001-7263-318X
Jian Ru Gong: 0000-0003-1512-4762

Author Contributions

#Y.D., P.C., and G.X. contributed equally to this work. The manuscript was written through contributions of all authors. All authors have given approval to the final version of the manuscript.

Notes

The authors declare no competing financial interest.

ACKNOWLEDGMENTS

This work was supported by the National Natural Science Foundation of China (21422303, 21573049, 21872043, 81602643, 11672079), the National Key R&D Program "nanotechnology" special focus (2016YFA0201600), the Beijing Natural Science Foundation (2142036), and the Knowledge Innovation Program, Youth Innovation Promotion Association, and Special Program of "One Belt One Road" of CAS. We thank Prof. Tao He and Dr. Yanjie Wang for their help with the IMPS measurements.

REFERENCES

(1) Khaselev, O.; Turner, J. A. A Monolithic Photovoltaic-Photoelectrochemical Device for Hydrogen Production Via Water Splitting. *Science* **1998**, *280*, 425−427.
(2) Chen, X.; Shen, S.; Guo, L.; Mao, S. S. Semiconductor-Based Photocatalytic Hydrogen Generation. *Chem. Rev.* **2010**, *110*, 6503−6570.
(3) Guo, B.; Tian, L.; Xie, W.; Batool, A.; Gong, J. R.; et al. Vertically Aligned Porous Organic Semiconductor Nanorod Array Photoanodes for Efficient Charge Utilization. *Nano Lett.* **2018**, *18*, 5954−5960.
(4) Yang, J.; Wang, D.; Han, H.; Li, C. Roles of Cocatalysts in Photocatalysis and Photoelectrocatalysis. *Acc. Chem. Res.* **2013**, *46*, 1900−1909.
(5) Guo, B.; Batool, A.; Xie, G.; Boddula, R.; Tian, L.; Jan, S. U.; Gong, J. R. Facile Integration between Si and Catalyst for High-Performance Photoanodes by a Multifunctional Bridging Layer. *Nano Lett.* **2018**, *18*, 1516−1521.
(6) Nellist, M. R.; Laskowski, F. A.; Lin, F.; Mills, T. J.; Boettcher, S. W. Semiconductor-Electrocatalyst Interfaces: Theory, Experiment, and Applications in Photoelectrochemical Water Splitting. *Acc. Chem. Res.* **2016**, *49*, 733−740.
(7) Ding, C.; Shi, J.; Wang, Z.; Li, C. Photoelectrocatalytic Water Splitting: Significance of Cocatalysts, Electrolyte, and Interfaces. *ACS Catal.* **2017**, *7*, 675−688.
(8) Jiao, Y.; Zheng, Y.; Jaroniec, M.; Qiao, S. Z. Design of Electrocatalysts for Oxygen- and Hydrogen-Involving Energy Conversion Reactions. *Chem. Soc. Rev.* **2015**, *44*, 2060−2086.
(9) Burke, M. S.; Enman, L. J.; Batchellor, A. S.; Zou, S.; Boettcher, S. W. Oxygen Evolution Reaction Electrocatalysis on Transition Metal Oxides and (Oxy)Hydroxides: Activity Trends and Design Principles. *Chem. Mater.* **2015**, *27*, 7549−7558.
(10) Chen, K.; Yang, Y.; Li, K.; Ma, Z.; Zhou, Y.; Xue, D. $CoCl_2$ Designed as Excellent Pseudocapacitor Electrode Materials. *ACS Sustainable Chem. Eng.* **2014**, *2*, 440−444.
(11) Klahr, B.; Gimenez, S.; Fabregat-Santiago, F.; Bisquert, J.; Hamann, T. W. Photoelectrochemical and Impedance Spectroscopic Investigation of Water Oxidation with "Co-Pi"-Coated Hematite Electrodes. *J. Am. Chem. Soc.* **2012**, *134*, 16693−16700.
(12) Liu, G.; Shi, J.; Zhang, F.; Chen, Z.; Han, J.; Ding, C.; Chen, S.; Wang, Z.; Han, H.; Li, C. A Tantalum Nitride Photoanode Modified with a Hole-Storage Layer for Highly Stable Solar Water Splitting. *Angew. Chem., Int. Ed.* **2014**, *53*, 7295−7299.
(13) Lin, F.; Boettcher, S. W. Adaptive Semiconductor/Electrocatalyst Junctions in Water-Splitting Photoanodes. *Nat. Mater.* **2014**, *13*, 81−86.
(14) Qiu, J.; Hajibabaei, H.; Nellist, M. R.; Laskowski, F. A.; Hamann, T. W.; Boettcher, S. W. Direct in Situ Measurement of Charge Transfer Processes During Photoelectrochemical Water Oxidation on Catalyzed Hematite. *ACS Cent. Sci.* **2017**, *3*, 1015−1025.
(15) Nellist, M. R.; Laskowski, F. A.; Qiu, J.; Hajibabaei, H.; Sivula, K.; Hamann, T. W.; Boettcher, S. W. Potential-Sensing Electrochemical Atomic Force Microscopy for in Operando Analysis of Water-Splitting Catalysts and Interfaces. *Nat. Energy* **2018**, *3*, 46−52.
(16) Liu, G.; Ye, S.; Yan, P.; Xiong, F.; Fu, P.; Wang, Z.; Chen, Z.; Shi, J.; Li, C. Enabling an Integrated Tantalum Nitride Photoanode to

Approach the Theoretical Photocurrent Limit for Solar Water Splitting. *Energy Environ. Sci.* **2016**, *9*, 1327−1334.
(17) Li, L.; Yang, X.; Lei, Y.; Yu, H.; Yang, Z.; Zheng, Z.; Wang, D. Ultrathin Fe-NiO Nanosheets as Catalytic Charge Reservoirs for a Planar Mo-Doped $BiVO_4$ Photoanode. *Chem. Sci.* **2018**, *9*, 8860−8870.
(18) Abel, A. J.; Patel, A. M.; Smolin, S. Y.; Opasanont, B.; Baxter, J. B. Enhanced Photoelectrochemical Water Splitting Via Silar-Deposited Ti-Doped Hematite Thin Films with an FeOOH Overlayer. *J. Mater. Chem. A* **2016**, *4*, 6495−6504.
(19) Le Formal, F.; Pastor, E.; Tilley, S. D.; Mesa, C. A.; Pendlebury, S. R.; Grätzel, M.; Durrant, J. R. Rate Law Analysis of Water Oxidation on a Hematite Surface. *J. Am. Chem. Soc.* **2015**, *137*, 6629−6637.
(20) Hajibabaei, H.; Schon, A. R.; Hamann, T. W. Interface Control of Photoelectrochemical Water Oxidation Performance with $Ni_{1-x}Fe_xO_y$ Modified Hematite Photoanodes. *Chem. Mater.* **2017**, *29*, 6674−6683.
(21) Thorne, J. E.; Jang, J.-W.; Liu, E. Y.; Wang, D. Understanding the Origin of Photoelectrode Performance Enhancement by Probing Surface Kinetics. *Chem. Sci.* **2016**, *7*, 3347−3354.
(22) Laskowski, F. A.; Nellist, M. R.; Qiu, J.; Boettcher, S. W. Metal Oxide/(Oxy)Hydroxide Overlayers as Hole Collectors and Oxygen Evolution Catalysts on Water Splitting Photoanodes. *J. Am. Chem. Soc.* **2019**, *141*, 1394−1405.
(23) Tsyganok, A.; Klotz, D.; Malviya, K. D.; Rothschild, A.; Grave, D. A. Different Roles of $Fe_{1-x}Ni_xOOH$ Cocatalyst on Hematite (α-Fe_2O_3) Photoanodes with Different Dopants. *ACS Catal.* **2018**, *8*, 2754−2759.
(24) Li, C.; Luo, Z.; Wang, T.; Gong, J. Surface, Bulk, and Interface: Rational Design of Hematite Architecture toward Efficient Photo-Electrochemical Water Splitting. *Adv. Mater.* **2018**, *30*, No. 1707502.
(25) Carroll, G. M.; Zhong, D. K.; Gamelin, D. R. Mechanistic Insights into Solar Water Oxidation by Cobalt-Phosphate-Modified α-Fe_2O_3 Photoanodes. *Energy Environ. Sci.* **2015**, *8*, 577−584.
(26) Carroll, G. M.; Gamelin, D. R. Kinetic Analysis of Photo-electrochemical Water Oxidation by Mesostructured Co-Pi/α-Fe_2O_3 Photoanodes. *J. Mater. Chem. A* **2016**, *4*, 2986−2994.
(27) Zhang, K.; Dong, T.; Xie, G.; Guan, L.; Guo, B.; Xiang, Q.; Dai, Y.; Tian, L.; Batool, A.; Jan, S. U.; et al. Sacrificial Interlayer for Promoting Charge Transport in Hematite Photoanode. *ACS Appl. Mater. Interfaces* **2017**, *9*, 42723−42733.
(28) Xu, Y. F.; Wang, X. D.; Chen, H. Y.; Kuang, D. B.; Su, C. Y. Toward High Performance Photoelectrochemical Water Oxidation: Combined Effects of Ultrafine Cobalt Iron Oxide Nanoparticle. *Adv. Funct. Mater.* **2016**, *26*, 4414−4421.
(29) Dong, Y.; He, K.; Yin, L.; Zhang, A. A Facile Route to Controlled Synthesis of Co_3O_4 Nanoparticles and Their Environmental Catalytic Properties. *Nanotechnology* **2007**, *18*, 435602−435607.
(30) Fominykh, K.; Tok, G. C.; Zeller, P.; Hajiyani, H.; Miller, T.; Döblinger, M.; Pentcheva, R.; Bein, T.; Fattakhova-Rohlfing, D. Rock Salt Ni/Co Oxides with Unusual Nanoscale-Stabilized Composition as Water Splitting Electrocatalysts. *Adv. Funct. Mater.* **2017**, *27*, 1605121−1605130.
(31) Kresse, G.; Furthmüller, J. Efficiency of Ab-initio Total Energy Calculations for Metals and Semiconductors Using a Plane-Wave Basis Set. *Comput. Mater. Sci.* **1996**, *6*, 15−50.
(32) Kresse, G.; Hafner, J. Ab initio Molecular Dynamics for Liquid Metals. *Phys. Rev. B* **1993**, *47*, 558.
(33) Kresse, G.; Hafner, J. Ab initio Molecular-Dynamics Simulation of the Liquid-Metal-Amorphous-Semiconductor Transition in Germanium. *Phys. Rev. B* **1994**, *49*, 14251.
(34) Kresse, G.; Joubert, D. Pseudopotentials to the Projector Augmented-Wave Method. *Phys. Rev. B* **1999**, *59*, 1758.
(35) Methfessel, M.; Paxton, A. T. High-Precision Sampling for Brillouin-Zone Integration in Metals. *Phys. Rev. B* **1989**, *40*, 3616.
(36) Wang, L.; Maxisch, T.; Ceder, G. Oxidation Energies of Transition Metal Oxides within the GGA+U Framework. *Phys. Rev. B* **2006**, *73*, 195107.
(37) Grimme, S. Semiempirical GGA-Type Density Functional Constructed with a Long-Range Dispersion Correction. *J. Comput. Chem.* **2006**, *27*, 1787−1799.
(38) Perdew, J. P.; Burke, K.; Ernzerhof, M. Generalized Gradient Approximation Made Simple. *Phys. Rev. Lett.* **1996**, *77*, 3865−3868.
(39) Rivas-Murias, B.; Salgueiriño, V. Thermodynamic CoO-Co_3O_4 Crossover Using Raman Spectroscopy in Magnetic Octahedron-Shaped Nanocrystals. *J. Raman Spectrosc.* **2017**, *48*, 837−841.
(40) Liao, L.; Zhang, Q.; Su, Z.; Zhao, Z.; Wang, Y.; Li, Y.; Lu, X.; Wei, D.; Feng, G.; Yu, Q.; et al. Efficient Solar Water-Splitting Using a Nanocrystalline CoO Photocatalyst. *Nat. Nanotechnol.* **2014**, *9*, 69−73.
(41) Yuan, X.; Ge, H.; Wang, X.; Dong, C.; Dong, W.; Riaz, M. S.; Xu, Z.; Zhang, J.; Huang, F. Controlled Phase Evolution from Co Nanochains to CoO Nanocubes and Their Application as OER Catalysts. *ACS Energy Lett.* **2017**, *2*, 1208−1213.
(42) Guan, J.; Ding, C.; Chen, R.; Huang, B.; Zhang, X.; Fan, F.; Zhang, F.; Li, C. CoO_x Nanoparticle Anchored on Sulfonated-Graphite as Efficient Water Oxidation Catalyst. *Chem. Sci.* **2017**, *8*, 6111−6116.
(43) Meher, S. K.; Rao, G. R. Ultralayered Co_3O_4 for High-Performance Supercapacitor Applications. *J. Phys. Chem. C* **2011**, *115*, 15646−15654.
(44) Zhong, D. K.; Cornuz, M.; Sivula, K.; Grätzel, M.; Gamelin, D. R. Photo-Assisted Electrodeposition of Cobalt-Phosphate (Co-Pi) Catalyst on Hematite Photoanodes for Solar Water Oxidation. *Energy Environ. Sci.* **2011**, *4*, 1759−1764.
(45) Wang, G.; Ling, Y.; Lu, X.; Zhai, T.; Qian, F.; Tong, Y.; Li, Y. A Mechanistic Study into the Catalytic Effect of $Ni(OH)_2$ on Hematite for Photoelectrochemical Water Oxidation. *Nanoscale* **2013**, *5*, 4129−4133.
(46) Zhang, J.; García-Rodríguez, R.; Cameron, P. J.; Eslava, S. Role of Cobalt-Iron (Oxy)Hydroxide ($CoFeO_x$) as Oxygen Evolution Catalyst on Hematite Photoanodes. *Energy Environ. Sci.* **2018**, *11*, 2972−2984.
(47) Malara, F.; Minguzzi, A.; Marelli, M.; Morandi, S.; Psaro, R.; Dal Santo, V.; Naldoni, A. α-Fe_2O_3/NiOOH: An Effective Heterostructure for Photoelectrochemical Water Oxidation. *ACS Catal.* **2015**, *5*, 5292−5300.
(48) Malara, F.; Fabbri, F.; Marelli, M.; Naldoni, A. Controlling the Surface Energetics and Kinetics of Hematite Photoanodes through Few Atomic Layers of NiO_x. *ACS Catal.* **2016**, *6*, 3619−3628.
(49) Klahr, B.; Gimenez, S.; Fabregat-Santiago, F.; Bisquert, J.; Hamann, T. W. Electrochemical and Photoelectrochemical Investigation of Water Oxidation with Hematite Electrodes. *Energy Environ. Sci.* **2012**, *5*, 7626−7636.
(50) Bertoluzzi, L.; Bisquert, J. Equivalent Circuit of Electrons and Holes in Thin Semiconductor Films for Photoelectrochemical Water Splitting Applications. *J. Phys. Chem. Lett.* **2012**, *3*, 2517−2522.
(51) Hagfeldt, A.; Gräetzel, M. Light-Induced Redox Reactions in Nanocrystalline Systems. *Chem. Rev.* **1995**, *95*, 49−68.
(52) Favaro, M.; Yang, J.; Nappini, S.; Magnano, E.; Toma, F. M.; Crumlin, E. J.; Yano, J.; Sharp, I. D. Understanding the Oxygen Evolution Reaction Mechanism on CoO_x Using Operando Ambient Pressure X-Ray Photoelectron Spectroscopy. *J. Am. Chem. Soc.* **2017**, *139*, 8960−8970.
(53) McAlpin, J. G.; Surendranath, Y.; Dinca, M.; Stich, T. A.; Stoian, S. A.; Casey, W. H.; Nocera, D. G.; Britt, R. D. EPR Evidence for Co (IV) Species Produced During Water Oxidation at Neutral pH. *J. Am. Chem. Soc.* **2010**, *132*, 6882−6883.
(54) Cong, X.; Cheng, C.; Liao, Y.; Ye, Y.; Dong, C.; Sun, H.; Ji, X.; Zhang, W.; Fang, P.; Miao, L.; Jiang, J. Intrinsic Charge Storage Capability of Transition Metal Dichalcogenides as Pseudocapacitor Electrodes. *J. Phys. Chem. C* **2015**, *119*, 20864−20870.
(55) Ji, X.; Xu, K.; Chen, C.; Zhang, B.; Wan, H.; Ruan, Y.; Miao, L.; Jiang, J. Different Charge-Storage Mechanisms in Disulfide Vanadium

DOI: 10.1021/acs.jpcc.9b08343
J. Phys. Chem. C 2019, 123, 28753−28762

and Vanadium Carbide Monolayer. *J. Mater. Chem. A* **2015**, *3*, 9909−9914.
(56) Ishii, H.; Sugiyama, K.; Ito, E.; Seki, K. Energy Level Alignment and Interfacial Electronic Structures at Organic/Metal and Organic/Organic Interfaces. *Adv. Mater.* **1999**, *11*, 605−625.
(57) Ling, T.; Yan, D.-Y.; Jiao, Y.; Wang, H.; Zheng, Y.; Zheng, X.; Mao, J.; Du, X.-W.; Hu, Z.; Jaroniec, M.; Qiao, S. Z. Engineering Surface Atomic Structure of Single-Crystal Cobalt (II) Oxide Nanorods for Superior Electrocatalysis. *Nat. Commun.* **2016**, *7*, No. 12876.
(58) Chen, J.; Selloni, A. Electronic States and Magnetic Structure at the Co_3O_4 (110) Surface: A First-Principles Study. *Phys. Rev. B* **2012**, *85*, No. 085306.
(59) Wang, D.; Sheng, T.; Chen, J.; Wang, H.-F.; Hu, P. Identifying the Key Obstacle in Photocatalytic Oxygen Evolution on Rutile TiO_2. *Nat. Catal.* **2018**, *1*, 291−299.
(60) Xie, G.; Guan, L.; Zhang, L.; Guo, B.; Batool, A.; Xin, Q.; Boddula, R.; Jan, S. U.; Gong, J. R. Interaction-Dependent Interfacial Charge Transfer Behavior in Solar Water Splitting Systems. *Nano Lett.* **2019**, *19*, 1234−1241.

DOI: 10.1021/acs.jpcc.9b08343
J. Phys. Chem. C 2019, 123, 28753−28762